Impact of platinum loading and dispersion on the catalytic activity of Pt/SnO_2 and $Pt/\alpha\text{-}Fe_2O_3$

I. Marić[1], G. Dražić[2], E. Radin[3], R. Peter[4], M. Škrabić[5], T. Jurkin[1], A. Pustak[1], N. Baran[3], L. Mikac[3], M. Ivanda[3], M. Petravić[4], G. Štefanić[3,*], M. Gotić[3,*]

[1]Radiation Chemistry and Dosimetry Laboratory, Ruđer Bošković Institute, Bijenička c. 54, 10000 Zagreb, Croatia
[2]National Institute of Chemistry, Hajdrihova 19, SI-1001, Ljubljana, Slovenia
[3]Laboratory for Molecular Physics and Synthesis of New Materials, Ruđer Bošković Institute, Bijenička c. 54, 10000 Zagreb, Croatia
[4]University of Rijeka, Department of Physics, Radmile Matejčić 2, Rijeka, Croatia
[5]Department of Physics and Biophysics, School of Medicine, University of Zagreb, Šalata 3b, 10000 Zagreb, Croatia

* Correspondence: Marijan.Gotic@irb.hr (M.G.) and Goran.Stefanic@irb.hr (G. Š.)

Abstract

The Pt/SnO_2 (SP-samples) and $Pt/\alpha\text{-}Fe_2O_3$ (FP-samples) with platinum loadings between 1 and 10 mol% were synthesized mechanochemically starting from platinum(II) acetylacetonate dissolved in toluene and from SnO_2 and $\alpha\text{-}Fe_2O_3$ powders obtained from tin(II) and iron(II) acetates. In addition to cassiterite (SnO_2), a small amount of Sn and Sn_2O_3 was found in SP-samples using XRD. The FP-samples consisted exclusively of $\alpha\text{-}Fe_2O_3$. The platinum maxima were not found in the XRD patterns of any sample, even at the highest platinum loading of 10 mol%. The STEM results show that the ultrasmall platinum nanoparticles (PtNPs) are well dispersed on the SnO_2 and $\alpha\text{-}Fe_2O_3$ supports. The PtNPs size distributions calculated with lognormal functions ranged from 1.0 to 1.3 nm. The main difference between the Pt dispersion on SnO_2 supports and $\alpha\text{-}Fe_2O_3$ supports is the presence of very small spots of about 0.1 nm in size, indicating a region of atomically dispersed platinum in the Pt/SnO_2 sample with 5 mol% Pt, while such regions were not found in the $Pt/\alpha\text{-}Fe_2O_3$ samples. The results of temperature programmed reduction in hydrogen showed maxima at 120-160 °C due to the reduction of PtO_x to Pt^0. The Pt-4f-XPS results showed that the dispersed platinum on the SnO_2 and $\alpha\text{-}Fe_2O_3$ supports consisted of all three oxidation states of platinum: Pt^{4+}, Pt^{2+} and Pt^0. The platinum on SnO_x and $\alpha\text{-}Fe_2O_3$ supports showed high catalytic activity for the reduction of 4-nitropenol (4-NP) to 4-aminophenol (4-AP), which can be explained by the high dispersion of non-aggregated ultrasmall PtNPs with a size of about 1 nm on the SnO_x and $\alpha\text{-}Fe_2O_3$ supports. The optimal platinum loading for the reduction of 4-NP to 4-AP on a SnO_2 support is 1 mol% with an apparent rate constant $k = 1.53 \times 10^{-2}\ s^{-1}$, while on a $\alpha\text{-}Fe_2O_3$ support the optimal platinum loading is 5 mol% with $k = 1.11 \times 10^{-2}\ s^{-1}$ if we assume pseudo-first order kinetics.

Keywods: platinum; dispersion; XPS; ball-milling; reducible supports; catalytic; 4-nitrophenol

1. Introduction

Platinum is a well-known catalyst that can also be used in electrochemistry and gas sensing. One of the most important parameters for platinum applications is its dispersion. The dispersion of platinum may be defined as the ratio between the number of atoms available for specific applications and the total number of platinum atoms. Platinum can be prepared in the form of platinum nanoparticles (PtNPs) dispersed in an aqueous or organic medium, or it can be dispersed on various supports [1-17]. PtNPs dispersed in a medium can coalesce, and generally the subnanometric PtNPs are difficult to stabilize in a liquid medium. In contrast, small PtNPs or atomic platinum can be dispersed on supports for various applications. For example, PtNPs dispersed on $\alpha\text{-}Fe_2O_3$ has been used as a photoanode in photoelectrochemical (PEC) experiments for water splitting [3]. Rangasamy et al [4] synthesized Pt-decorated magnetite-poly(epoxyamine) nanocomposites, which proved to be efficient catalysts for the

reduction of p-nitrophenol to p-aminophenol. Ouyang et al [5] reported an in situ preparation strategy for well-dispersed, ligand-free Pt nanoclusters (1.28 nm) supported on carbon spheres for the catalytic dehydrogenation of methylcyclohexane at high temperatures without the need for pretreatments for deoxidation. Cai et al [6] synthesized Pt-doped SnO_2 nanospheres with mesoporous hollow structure and used them for the detection of 3-hydroxy-2-butanone biomarker of L. monocytogenes, a life-threatening foodborne pathogen. The hollow hybrid particles with small platinum clusters on their surface were synthesized [7] by mild reduction of platinum salts with pentaerythritol tetrakis-mercaptopropionate. Bulemo et al [8] synthesized PtNPs by the polyol reduction method and then functionalized SnO_2 hollow spheres (HSPs) with the obtained PtNPs. The Pt-SnO_2 HSPs were used as gas sensing materials with excellent response and selectivity for H_2S. Martyla et al [9] synthesized a Pt/SnO_2 electrocatalyst using a one-pot sol-gel method. The Pt/SnO_2-based electrocatalyst showed electrochemical activity in the oxidation of methanol in acidic solution. Kocemba et al [10] studied the influence of catalytic activity on the response of Pt/SnO_2 gas sensors to carbon monoxide and hydrogen. It was found that the catalytic activity in the oxidation of CO and the sensitivity of Pt/SnO_2 sensors to CO do not change in parallel. Tellez-Cruz [11] studied the influence of functionalized Vulcan and Black Pearl carbons on the specific and mass activities of Fe_2O_3-Pt catalysts for the oxygen reduction reaction (ORR). The synthesized Fe_2O_3-Pt particle catalyst on Vulcan carbon showed higher mass activity for the oxygen reduction reaction compared to a Black Pearl carbon support. An et al. [12] studied the catalytic properties of platinum catalysts on iron oxide supports (Pt/Fe_2O_3) prepared by colloidal deposition for the complete oxidation of formaldehyde. It was suggested that the presence of a suitable interaction between Pt particles and iron oxide supports, mainly in the form of Pt-O-Fe bonds, should play a positive role in determining the catalytic activity and stability of the supported Pt/Fe_2O_3 catalysts. Rachmady and Vennice [13] studied the catalytic behaviour of hydrogenation of acetic acid over Pt on TiO_2, SiO_2, α-$A1_2O_3$, and Fe_2O_3. The interaction of acetic acid with the oxide support played an important role in determining the reaction kinetics, and the main role of Pt in this case was to serve as a source of mobile activated hydrogen atoms. Wang et al. [14] used 2, 4, 6, and 8 nm platinum nanoparticles on mesoporous silica as catalysts to study the size effect, and 2.5 nm platinum nanoparticles on mesoporous SiO_2, Co_3O_4, MnO_2, Fe_2O_3, NiO, and CeO_2 to study the metal/oxide interface effect. It was found that the reaction rates in the gas phase were drastically affected by the strong interactions between the platinum nanoparticles and the transition metal oxide supports. Dai et al. [15] reported that the electronic structure and dispersion of PtNPs can be modified by the supports. It was found that the Pt/ α-Fe_2O_3 catalyst exhibited superior catalytic performance for hydrogenation of 3-nitrostyrene because of its low coordinated Pt sites and the small PtNPs size.

In contrast to typical wet chemical processes such as impregnation or co-precipitation, Schreyer et al. [16] reported dry ball milling of macroscopic metal powder in the presence of a support oxide for the synthesis of catalysts on metal supports with particle sizes in the nanometer range. Different supports, including TiO_2, Al_2O_3, Fe_2O_3, and Co_3O_4, and different metals such as Au, Pt, Ag, Cu, and Ni were investigated, and highly dispersed nanoparticles on supports were prepared for each support and metal. The supported catalysts were tested in the oxidation of CO, where they showed activities in the same range as conventionally prepared catalysts.

In a previous work [17] we mechanochemically dispersed Pt on SnO_2 and α-Fe_2O_3 supports in three ways *(i)* in one step by mixing powdered Fe (II) acetate or Sn (II) acetate precursor with platinum (II) acetylacetonate, *i.e.* Pt(acac)$_2$ in a planetary mill followed by annealing at 600 °C; *(ii)* in two steps, where first α-Fe_2O_3 and SnO_2 were synthesized at 600 °C, and then in the second step the pristine powder samples were mixed with Pt(acac)$_2$ powder and homogenized in a planetary mill and annealed at 400 °C; *(iii)* in two steps, where first α-Fe_2O_3 and SnO_2 were synthesized at 600 °C and then in the second step the pristine powder samples were mixed with Pt(acac)$_2$ previously dissolved in toluene and

then the obtained paste was homogenized in a planetary mill and annealed at 400 °C. We found that the size of the dispersed PtNPs over α-Fe_2O_3 depended on the experimental conditions and that a two-step process in which the $Pt(acac)_2$ was previously dissolved in toluene yielded the smallest PtNPs. However, the effects of the Pt loadings and the catalytic properties of Pt/SnO_2 and Pt/α-Fe_2O_3 were not studied. It can be assumed that higher Pt loading, i.e., using a larger amount of catalyst, would have a positive effect on the catalytic properties of platinum. On the other hand, it is known that it is very difficult to disperse large amounts of catalyst on supports because the particles can aggregate. Therefore, we assume that there is an optimal Pt loading where the size, concentration, and dispersion of PtNPs on supports have the best catalytic properties. Another question that arises is whether this optimal Pt loading is the same for different supports such as reducible α-Fe_2O_3 and SnO_2 supports. Thus, Pt loading is important not only because of the cost of the catalyst, but also because of the relationship between dispersion and catalytic properties as a function of Pt loading. In addition to the above reasons, the study of Pt loading is very important for the microstructural and physicochemical characterization of the catalyst, since low Pt loading is not sufficient to determine, for example, the unit cell parameters. In previous work, we assumed the formation of $(Pt,Sn)O_2$ solid solution, but to confirm or exclude the formation of solid solution beyond doubt, we should have a certain range of Pt loadings to determine the change of unit cell parameters.

In this work, we mechanochemically dispersed 1, 3, 5, and 10 mol% platinum dissolved in toluene over reducible SnO_2 and α-Fe_2O_3 supports and studied the platinum dispersions, physicochemical properties, and catalytic properties of Pt/SnO_2 and Pt/α-Fe_2O_3 for the reduction of 4-nitrophenol (4-NP) to 4-aminophenol (4-AP).

2. Materials and Methods

2.1 Chemicals

Iron(II) acetate (Cat. No. 517933), tin(II) acetate (Product. No. 345164), platinum(II) acetylacetonate (Product. No. 282782) and anhydrous toluene (Product. No. 244511) produced by Sigma Aldrich, were used as received. Chemicals used for catalytic experiments were: 4-nitrophenol - Sigma Aldrich, Reagent Plus, ≥99%, CAS: 100-02-7, Product No: 241326 and sodium borohydrate ($NaBH_4$) - Alfa Aesar, min.98%, CAS: 16940-66-2, Product No.: 88983. Deionized Milli-Q water was used in catalytic experiments.

2.2 Synthesis of the samples

The untreated hematite (α-Fe_2O_3) sample was synthesized by grinding Fe(II) acetate in a planetary mill "FRITSCH PULVERISETTE 7 premium line" with 40 balls of hardened stainless steel (Fe - Cr No. 55.0100.09) of size 5 mm at a speed of 400 rpm for two hours. After grinding, the obtained orange-red powder was put in a tube furnace for 30 min in an argon stream at 200 °C, 30 min in an argon stream at 400 °C, 1 hour in an argon stream at 600 °C and 2 hours in an oxygen stream at 600 °C; a dark red powder was obtained, which was assigned as a **sample FP-0**.

The untreated tin oxide (cassiterite) sample was synthesized in the same manner as hematite sample FP-0, except that the starting chemical was tin(II) acetate instead of iron(II) acetate. A white powder was obtained and assigned as **sample SP-0**.

Platinum was dispersed by mixing the untreated powder samples FP-0 and SP-0 with 1, 3, 5, and 10 mol% $Pt(acac)_2$ powder precursors previously dissolved in a given volume of toluene. The paste obtained was homogenized in a planetary mill at a speed of 400 rpm for 2 hours with 5 mm stainless steel balls and annealed in an argon stream for one hour and in an oxygen stream at 400 °C for two hours. Samples are designated as **SP-1, SP-3, SP-5, and SP-10 and FP-1, FP-3, FP-5, and FP-10**,

where S represents SnO_2, F represents α-Fe_2O_3, P represents platinum, and the numbers 1, 3, 5, and 10 represent 1, 3, 5, and 10 mol% Pt in the sample, respectively.

2.3 Instrumental analysis

X-ray diffraction (XRD) measurements were performed at room temperature using APD 2000 diffractometer (CuKα radiation, graphite monochromator, NaI-Tl detector) manufactured by ITALSTRUCTURES, Riva Del Garda, Italy.

Atomic resolution scanning transmission electron microscope (AR STEM), model Jeol ARM 200 CF, with voltage emission of 200 kV coupled with Gatan Quantum ER system and with electron energy loss spectroscopy and energy dispersive x-ray spectrometry (Jeol Centurio 100) was used.

Nitrogen adsorption measurements at 77 K for Brunauer-Emmett-Teller (BET) analysis and necessary degassing pre-treatment were done on Quantachrome Autosorb iQ3 system. Prior to the measurement, the material was kept at 250 °C under vacuum to remove any residual gas and moisture from the sample. This was performed until the rate of rise of pressure with closed vacuum valves was less than 50 millitorr per minute. The adsorption-desorption isotherms were measured at 77 K in a relative pressure range of ~10^{-5} to ~0.99.

Temperature-programmed reduction (TPR) experiments were performed using a Quantachrome Autosorb iQ3-AG-C instrument. In a typical experiment, 100 mg of sample was placed in a quartz tube and the temperature was raised from room temperature to 120 °C in a stream of helium at a constant rate of 20 °C/min. The sample temperature was maintained at 120 °C for 40 minutes and then cooled to 40 °C. The sample was then heated to 800 °C under a reducing gas mixture (10% H_2 / 90% Ar) at a rate of 10 °C/min. A thermal conductivity detector (TCD) was used to measure the changes in thermal conductivity of the effluent gas. At the end of the measurements, the samples were cooled in a stream of nitrogen.

X-ray photoelectron spectroscopy (XPS) was used to study chemical composition of Fe and Sn powder samples loaded with Pt. The spectra around Fe 2p, Sn 3d and Pt 4f core levels were recorded with a SPECS instrument under ultra-high vacuum (UHV) conditions (the typical pressure in the analysis chamber was in the range of 10^{-7} Pa) with an excitation energy of 1486.74 eV (Al Kα X-rays) and the Phoibos100 electron energy analyzer. The charge stabilization on nonconductive oxide samples was obtain by flooding the sample surfaces during XPS analysis with the 5 eV electrons. The pass energy was set to 50 eV for the measurements around the Pt 4f core levels, while the spectra around Fe 2p and Sn 3d levels were recorded with the pass energy of 10 eV. Numerical fitting of the experimental curves was performed with the Unifit software [18], using the mixture of Gaussian and Lorentzian functions. All photoemission spectra were calibrated against the C 1s peak set at the binding energy (BE) of 284.5 eV.

UV-Vis reflectance spectra were collected with a Shimadzu UV/VIS/NIR spectrometer, model UV-3600. The used wavelength range was from 1200 to 200 nm.

2.4 Catalytic measurements

Catalytic reduction of 4-nitrophenol (4-NP) to 4-aminophenol (4-AP) was studied by UV-Vis spectrophotometry in the presence of the synthesized samples and $NaBH_4$. 4-Nitrophenol and $NaBH_4$ solutions were not purged with N_2 prior to catalytic measurements. The aqueous $NaBH_4$ solution was freshly prepared before each experiment. Typically, 1 mg of the synthesized sample was dispersed in 25 mL of aqueous 4-nitrophenol solution ($0.4 \times \cdot 10^{-3}$ mol dm^{-3}) using an ultrasonic bath. This suspension was then mixed with 25 mL of aqueous $NaBH_4$ solution (0.16 mol dm^{-3}) and stirred continuously with a magnetic stirrer. Immediately after the addition of the synthesized samples, the UV-Vis absorption

spectra were recorded at time intervals until the maximum of nitrophenolate ions disappeared at 400 nm. The formation of 4-AP was followed by an increase in the maximum at 300 nm.

3. Results

3.1. XRD results

Fig. 1 shows the results of Rietveld refinement of the XRD patterns of samples SP-5 and FP-5. The results of the Rietveld refinements of the other samples are given in **Fig. S1** in the Supplementary materials. The observed and calculated patterns are indicated by diamond dots and red solid lines, while the differences between the observed and calculated patterns are indicated by blue lines in the lower panel. The calculated diffraction patterns of the cassiterite phase (sample SP-5) and the hematite phase (sample FP-5), as well as the LaB_6 standard, are shown in the boxes below the patterns. In the case of sample SP-5, the diffraction lines of the cassiterite phase show bimodal size distributions fitted with two different profile functions, one for narrow (SnO_2 (1)) and one for broad (SnO_2 (2)) diffraction lines.

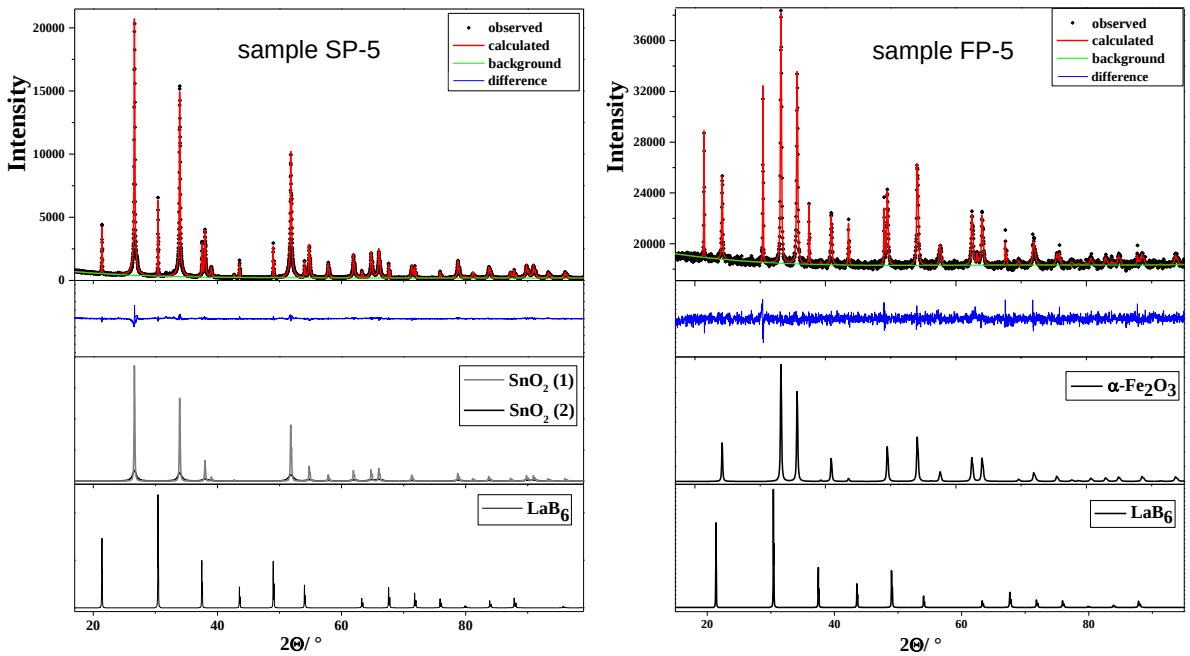

Fig. 1 The results of Rietveld refinement of the XRD patterns of samples SP-5 and FP-5. The results of the Rietveld refinements of the other samples are given in the Supplementary materials.

In addition to cassiterite, a small amount of Sn was found in sample SP-0 and Sn_2O_3 in samples SP-1 to SP-10 (Table 1). The XRD patterns with distinct maxima for these minor phases are shown in **Fig. S2** in the Supplementary materials. The FP-samples consist entirely of α-Fe_2O_3 (Table 2). The platinum maxima were not found in any XRD pattern even at the highest platinum loadings of 10 mol% (samples SP-10 and FP-10). The values of unit-cell parameters and volume averaged domain size (D_v) of cassiterite in the SP-samples and hematite in the FP-samples, obtained from the results of Rietveld refinements (software MAUD) with added LaB_6 as an internal standard are given in Table 3 and Table 4, respectively. The unit-cell parameter values of cassiterite in the SP-samples (Table 3) and hematite in the FP-samples (Table 4) did not change with Pt loading, confirming that there was no substitution

of Sn^{4+} or Fe^{3+} by Pt^{4+} in cassiterite or hematite, respectively. The Rietveld refinement results revealed two domain sizes (D_v) of cassiterite in the SP-samples, the larger one (D_{v1}) with a volume averaged domain sizes >100 nm and the smaller D_{v2} with values of about 10 nm (Table 3). The volume averaged sizes of hematite ranged from 60 to 90 nm (Table 4).

Table 1 The results of phase analysis of the samples SP-0, SP-1, SP-3 , SP-5 and SP-10.

Sample	Phase
SP-0	*t*-SnO_2 + Sn (traces)
SP-1	*t*-SnO_2 + Sn_2O_3 (~1%)
SP-3	*t*-SnO_2 + Sn_2O_3 (~2%)
SP-5	*t*-SnO_2 + Sn_2O_3 (~1%)
SP-10	*t*-SnO_2 + Sn_2O_3 (~2%)

Description: *t*-SnO_2 = phase structurally closely related to cassiterite; Sn = phase structurally closely related to tetragonal tin described in reference [1]; Sn_2O_3= phase structurally closely related to triclinic tin-oxide described in reference [2].

Table 2 The results of phase analysis of the samples FP-0, FP-1, FP-3, FP-5 and FP-10.

Sample	Phase
FP-0	α-Fe_2O_3
FP-1	α-Fe_2O_3
FP-3	α-Fe_2O_3
FP-5	α-Fe_2O_3
FP-10	α-Fe_2O_3

Description: α-Fe_2O_3 = phase structurally closely related to hematite.

Table 3 The values of unit-cell parameters and volume averaged domain size (D_v) of the cassiterite in the samples SP-0, SP-1, SP-3, SP-5 and SP-10, as determined from the results of Rietveld refinements (program MAUD) of samples with added LaB_6 as internal standard.

Sample	Phase	Rietveld refinement			
		Unit-cell parameters/ nm	D_{v1}/ nm	D_{v2}/ nm	R_{wp}
SP-0	Cassiterite	*a* = 0.47380(1); *c* = 0.31867(1)	>100	10(2)	0.058
SP-1	Cassiterite	*a* = 0.47382(1); *c* = 0.31867(1)	>100	8(2)	0.075
SP-3	Cassiterite	*a* = 0.47379(1); *c* = 0.31867(1)	>100	9(2)	0.087
SP-5	Cassiterite	*a* = 0.47380(1); *c* = 0.31868(1)	>100	11(2)	0.076
SP-10	Cassiterite	*a* = 0.47379(1); *c* = 0.31867(1)	>100	9(2)	0.088

Description: D_{v1} and D_{v2} stand for two different values of volume averaged domain size of cassiterite.

Table 4 The values of unit-cell parameters and volume averaged domain size (D_v) of the hematite phase in the samples FP-0, FP-1, FP-3, FP-5 and FP-10, as determined from the results of Rietveld refinements (program MAUD) of samples with added LaB_6 as internal standard.

Sample	Phase	Rietveld refinement		
		Unit-cell parameters/ nm	D_v/ nm	R_{wp}
FP-0	Hematite	*a* = 0. 50373(1); *c* = 1.37587(3)	75(5)	0.019
FP-1	Hematite	*a* = 0. 50379(1); *c* = 1.37633(5)	60(5)	0.022
FP-3	Hematite	*a* = 0. 50380(1); *c* = 1.37628(4)	60(5)	0.014
FP-5	Hematite	*a* = 0. 50373(1); *c* = 1.37589(3)	75(5)	0.013

FP-10	Hematite	a = 0. 50364(1); c = 1.37563(4)	90(5)	0.025

3.2. STEM results

Fig. 2 shows STEM dark field (DF) images of samples SP-1, SP-5, SP-10, FP-1, FP-5, and FP-10. Each sample is shown with one large image and two smaller images arranged below the large image. Numerous bright spots are seen, characteristic of very small nanometric PtNPs on much larger particles. The DF images of sample SP-5 (scale on the image 5 and 2 nm) show numerous very small bright spots indicative of atomically dispersed platinum.

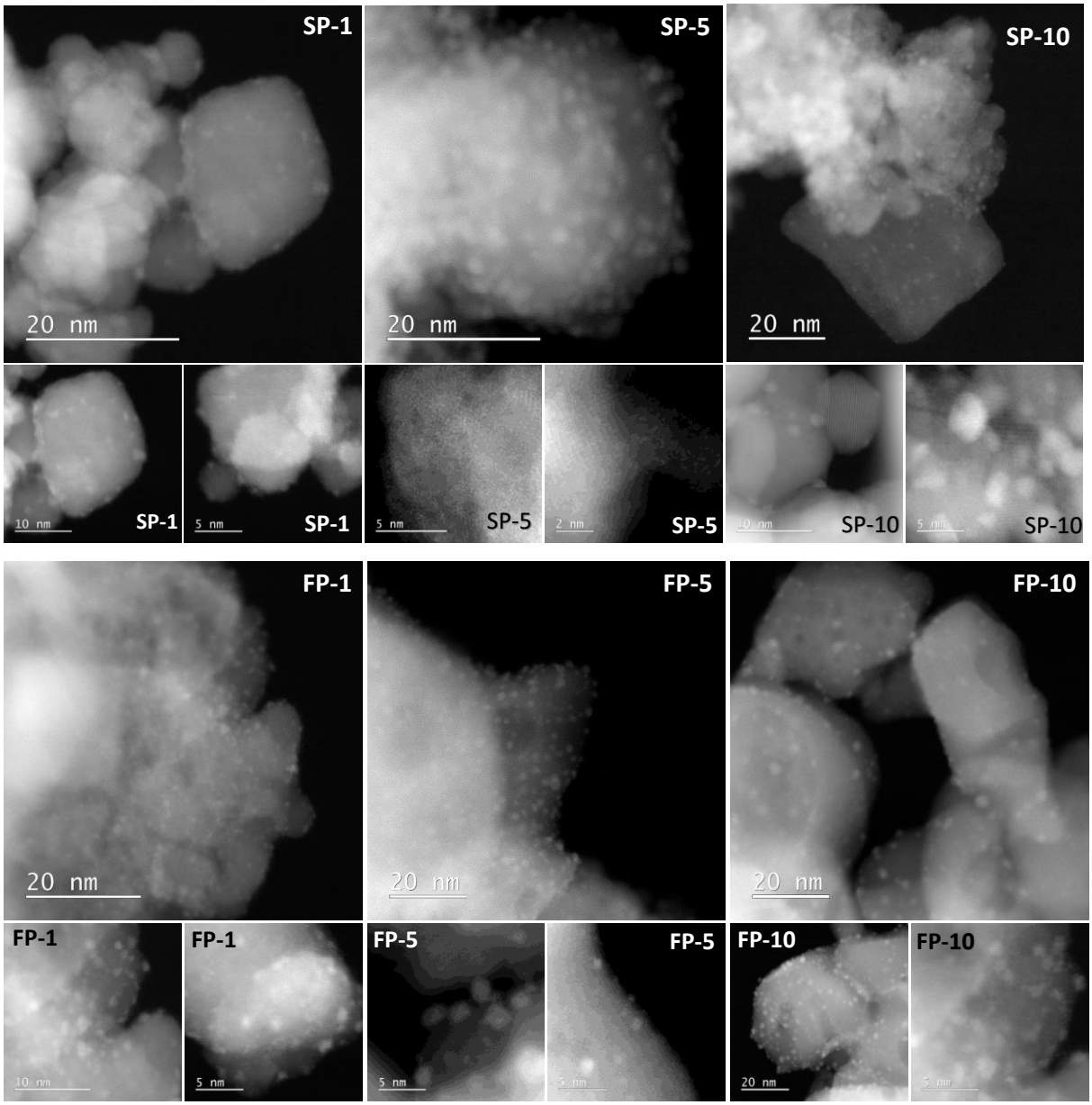

Fig. 2 shows STEM dark field (DF) images of samples SP-1, SP-5, SP-10, FP-1, FP-5, and FP-10. Each sample is shown with one large image and two smaller images arranged below the large image.

Fig. 3 shows the size distributions of the platinum particles calculated using the normal and lognormal functions from the images shown in Fig. 2.

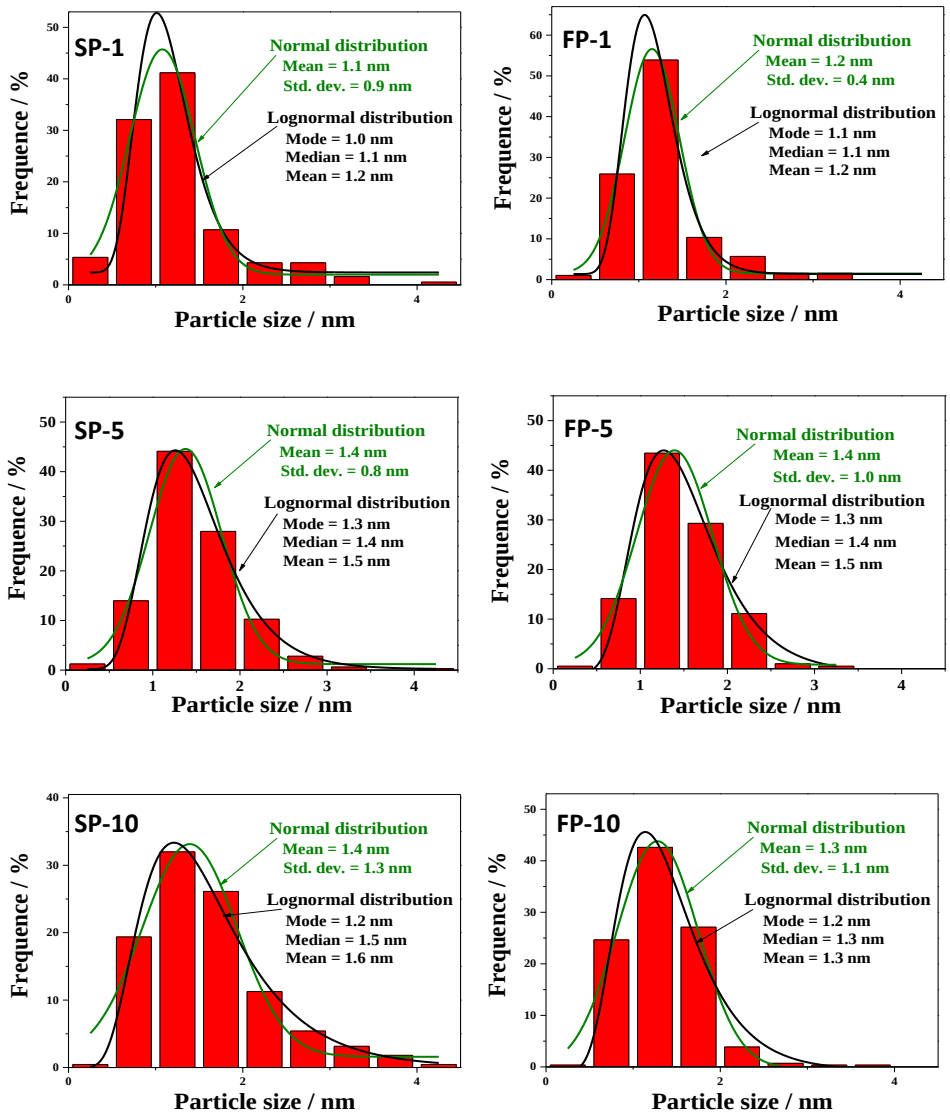

Fig. 3 The size distributions of the platinum particles calculated using the normal and lognormal functions from the images shown in Fig. 2.

Fig. 4 shows a STEM image and EDXS analysis of sample SP-1 (upper panel) and sample SP-10 (lower panel). The corresponding EDXS elemental mapping images of the Sn L edge (a), the O K edge (b), the Fe K edge (c), the Pt M edge (d), and the overlay of the Sn L, O K, Fe K, and Pt M edges (e) show a fairly homogeneous distribution of all elements in the samples. The EDXS spectra shown in (f) detect platinum and a small amount of iron. The iron impurities are due to the stainless steel balls used in the synthesis of the sample in a high energy planetary mill. The EDXS elemental mapping images of sample SP-5 and FP-5 are shown in **Fig. S3** in the Supplementary Materials.

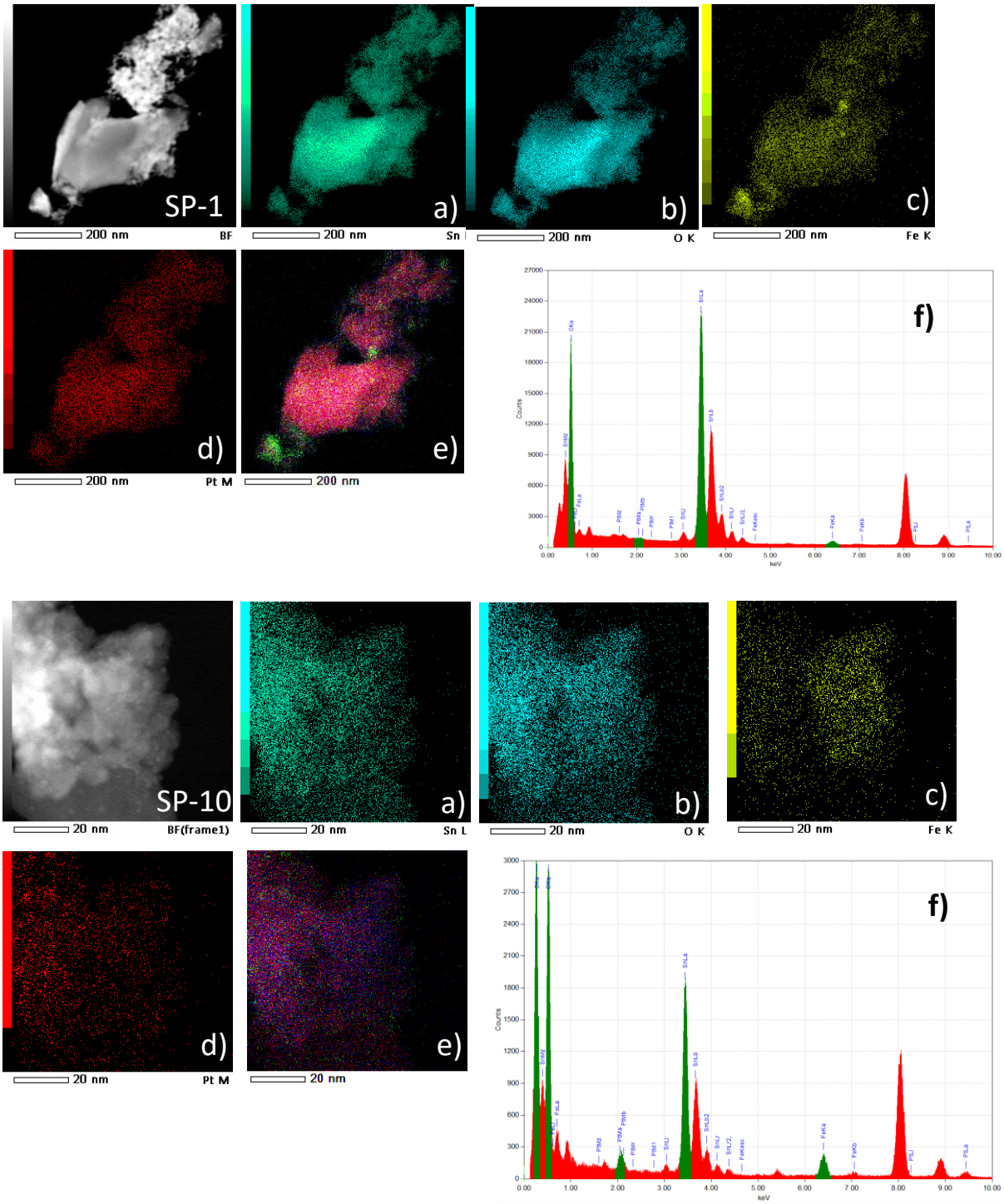

Fig. 4 STEM image of sample SP-1 (top panel) and the corresponding EDXS elemental mapping images of the Sn L edge (a), O K edge (b), Fe K edge (c), Pt M edge (d), and the overlay of the Sn L, O K, Fe K, and Pt M edges (e). The EDXS spectrum shown in (f) confirms the presence of platinum and contains a small amount of iron. The bottom panel shows the STEM image of the sample SP-10 and the corresponding EDXS elemental mapping images of the Sn L edge (a), O K edge (b), Fe K edge (c), Pt M edge (d), and the overlay of the Sn L, O K, Fe K, and Pt M edges (e). The EDXS spectrum shown in (f) detects platinum and iron due to the to the stainless steel balls used in the synthesis.

3.3. BET nitrogen adsorption-desorption isotherm

Fig. 5 shows the gas (N_2) adsorption (red line, circle) and desorption (blue line, squares) isotherms of the samples SP-0 to SP-10 and FP-0 to FP-10. The samples show the reversible physisorption isotherm of the type II. The calculated Brunauer, Emmett, and Teller (BET) specific surface areas for the SP-samples show a decrease in the BET surface area from 23.4 $m^2 g^{-1}$ in the SP-0 sample to 13.6 $m^2 g^{-1}$ in the SP-10 sample. For the FP-samples, the BET surface area decreases with platinum loading from 33.4 to 14.0 $m^2 g^{-1}$. In general, the FP-samples have a slightly larger BET surface area compared to the SP-samples.

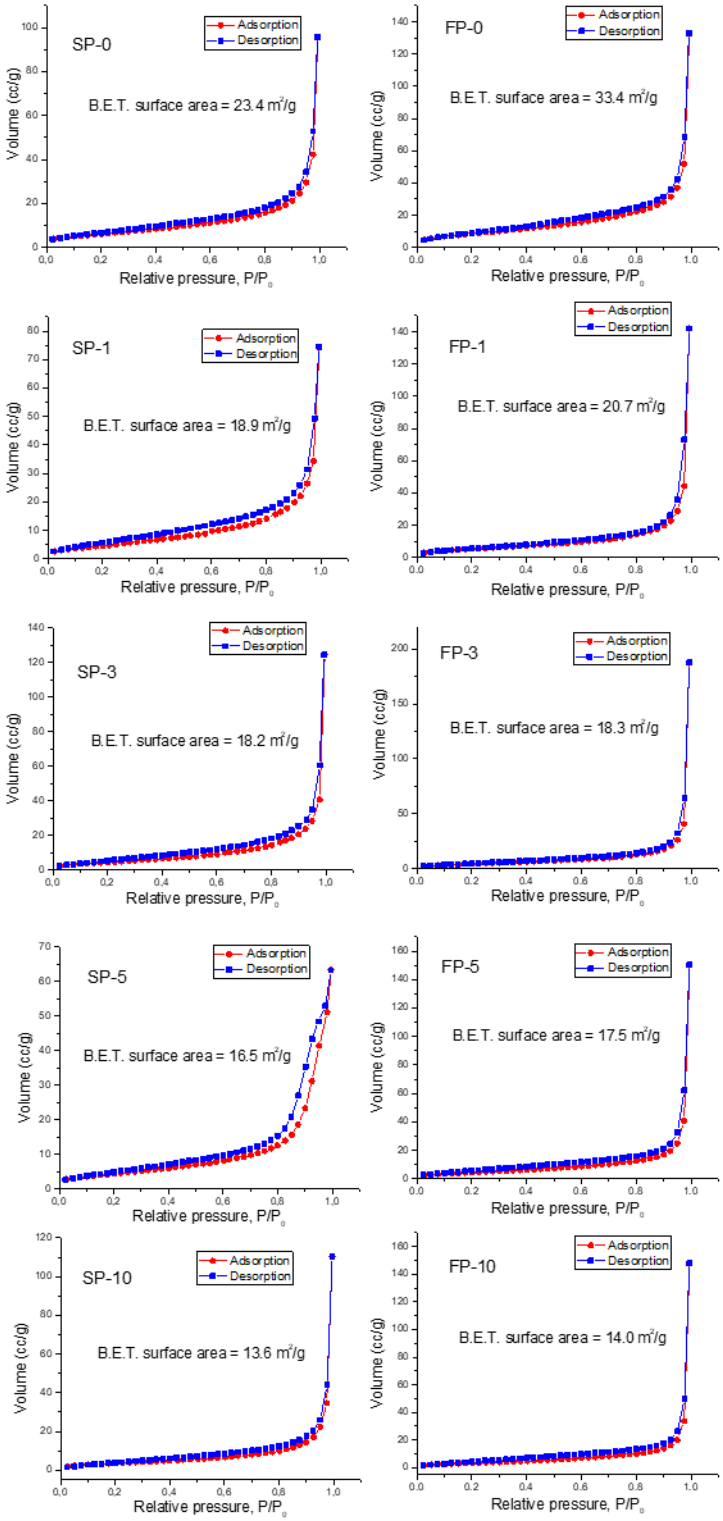

Fig. 5 Gas (N_2) adsorption (red line, circle) and desorption (blue line, squares) isotherms and calculated BET surface areas of synthesized samples.

3.4. TPR results

Fig. 6 shows the results of Temperature Programmed Reduction in hydrogen (H_2-TPR). The H_2-TPR curve of the sample SP-0, to which no platinum was added, shows two maxima, a very low

maximum at 283 °C and an incomplete maximum at 740 °C. The incomplete reduction of SnO_x to Sn can be attributed to the formation of the SnO and/or Sn metal shell around the SnO_2 particles. The melting point of tin is very low at 232 °C, so the molten tin on the surface of SnO_2 particles can protect Sn^{4+} from reduction. The addition of Pt catalyses the reduction of SnO_2, and in the sample SP-1 a well-defined maximum at 680 °C is due to the reduction of SnO_x to Sn^0. The very low and broad maximum at 121-159 °C, which is not present in the untreated sample SP-0, corresponds to the reduction of PtO_x to Pt^0. This maximum in the sample SP-3 is at 130-168 °C, in the sample SP-5 it is at 112 °C and is surprisingly narrow and intense, and in the sample SP-10 this maximum is at 162 °C due to the strong interaction of Pt and SnO_x. In the sample SP-10, also due to the high Pt loading and the strong interaction of Pt and SnO_x, a new strong maximum has appeared at 317 °C, which may be due to the formation of intermetallic compounds Sn_xPt_y. The fluctuation of the maximum from 680-740 °C due to the reduction of SnO_x to Sn^0 can be explained by the strong interaction of Pt and SnO_x and different Pt loadings.

The H_2-TPR curve of the sample FP-0, to which no platinum was added, shows two maxima, a maximum at 412 °C and a maximum at 643 °C. The first maximum at 421 °C corresponds to the reduction of α-$Fe_2O_3 \rightarrow Fe_3O_4$, and the second maximum at 643 °C corresponds to the reduction of $Fe_3O_4 \rightarrow FeO \rightarrow Fe$ [19]. Upon addition of 1 mol% platinum, sample FP-1, the maximum at 421 °C and 643 °C shifted to lower temperatures at 336 and 624 °C, respectively. The third maximum at 132 °C in sample FP-1, which is not present in the untreated sample FP-0, corresponds to the reduction of PtO_x to Pt^0. This maximum in samples FP-3 and FP-5 is at 147 °C and is relatively intense. In the sample FP-10, due to the high Pt loading, the PtO_x to Pt^0 maximum at 147 °C and α-Fe_2O_3 to Fe_3O_4 maximum at 334 °C shift to lower values at 128 °C and 277 °C, respectively. Moreover, at this high Pt loading, the relative intensity of the maximum of PtO_x to Pt^0 decreases, while the maximum at 277 °C becomes narrower and much more intense because the reduction of α-Fe_2O_3 to Fe_3O_4 is promoted. The position and shape of the maximum due to the reduction of Fe_3O_4 (FeO_x) to Fe^0 depends on the Pt loading and varies between 624 and 650 °C.

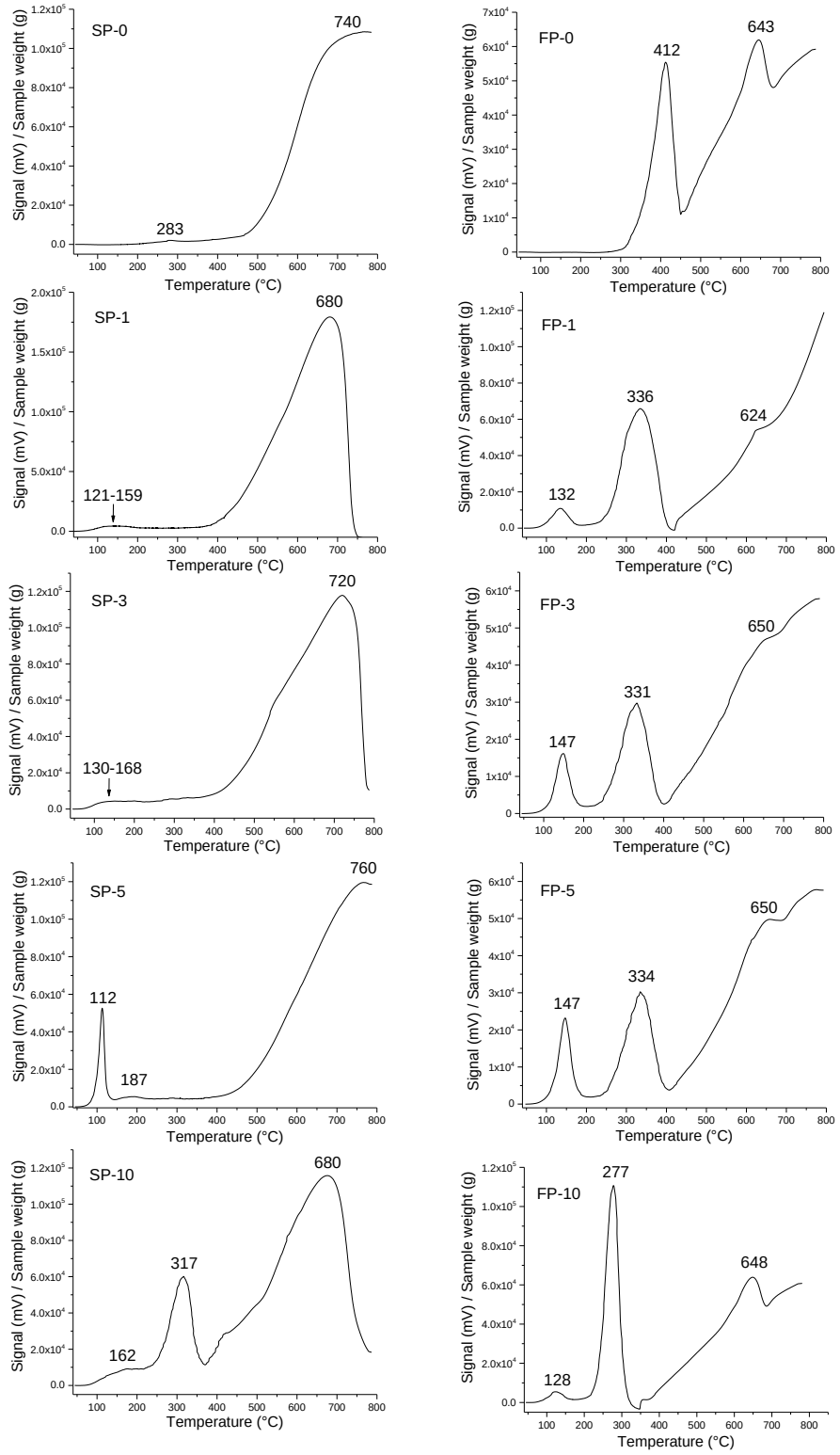

Fig. 6 The results of Temperature Programmed Reduction in hydrogen (H_2-TPR) for synthesized samples.

3.5. XPS results

Fig. 7 (left panel) shows the photoemission spectra around the Sn 3d core levels of the untreated tin oxide sample (SP-0), and the platinum loaded SnO_2 samples. All spectra are characterized with three spin-orbital doublets, related to the three different oxidation states of Sn, *i.e.* Sn^0, Sn^{2+} and Sn^{4+} [d,e,f], However, the contribution of tin atoms in the Sn^{4+} state (*i.e.* SnO_2) dominates all spectra with the Sn $3d_{5/2}$ peak at BE of 486.7 eV and the $3d_{3/2}$ peak shifted by 8.4 eV toward the higher BE [20,21].-**Fig. 11** (right panel) shows the XPS spectra of the hematite powders around Fe 2p core-levels. All samples, the untreated FP-0 and the platinum-treated samples, show the photoemission curves characteristic of α-Fe_2O_3: broad and asymmetric Fe $2p_{3/2}$ and Fe $2p_{1/2}$ spin-orbital doublets centered at the BEs of 710.8 eV and 724.0 eV, respectively, with the presence of the expected satellite peaks at 719.0 eV and 733.2 eV [22,23]. In all cases, however, the good fit of the experimental curves was possible only by introducing a small doublet with the components at 707.4 eV (Fe $2p_{3/2}$) and 720.5 eV (Fe $2p_{1/2}$). This doublet can be attributed to the presence of metallic Fe in the samples [24]. XPS wide spectra are shown in **Figs. S4 and S5** in the Supplementary materials.

Fig. 8 shows the Pt 4f photoemission curves of the SnO_2 and α-Fe_2O_3 samples loaded with platinum. All spectra are fitted with the three doublets, assigned to the platinum oxidation states Pt^0, Pt^{2+} and Pt^{4+}. The energy positions of the Pt $3d_{7/2}$ peaks are 70.8 eV (Pt^0), 72.5 eV (Pt^{2+}) and 74.5 eV (Pt^{4+}), while the energy separation between the Pt $3d_{7/2}$ and Pt $3d_{5/2}$ peaks is about 3.3 eV, for all Pt oxidation states, which is in good agreement with the data for platinum oxides from the literature [25,26]. The relative contributions of the Pt oxidation states, extracted from the fitted spectra, are also shown in Fig. 12. Our results indicate that the platinum dispersion on the SnO_2 and α-Fe_2O_3 supports gives presence to all three oxidation states of platinum (Pt^0, Pt^{2+} and Pt^{4+}). For example, among the SP-samples, the SP-5 sample has the highest Pt^0 content (34.3 %), whereas the SP-10 sample has the highest Pt^{4+} value (26.6 %). In general, the SP-samples contain a relatively higher percentage of Pt^0 and Pt^{2+} compared to the FP-samples, with the exception of the SP-1 and FP-1 samples. The highest Pt loading of 10 mol% Pt favours the oxidation conditions with the higher relative proportions of Pt^{4+}. The peak positions and relative proportions (%) of Pt^{4+}, Pt^{2+}, Pt^0, Sn^{4+}, Sn^{2+}, Sn^0, Fe^{3+} and Fe^0 in the synthesized samples based on the deconvoluted Pt 4f, Sn 3d and Fe 2p spectra are given in **Table S1** in the supplementary materials.

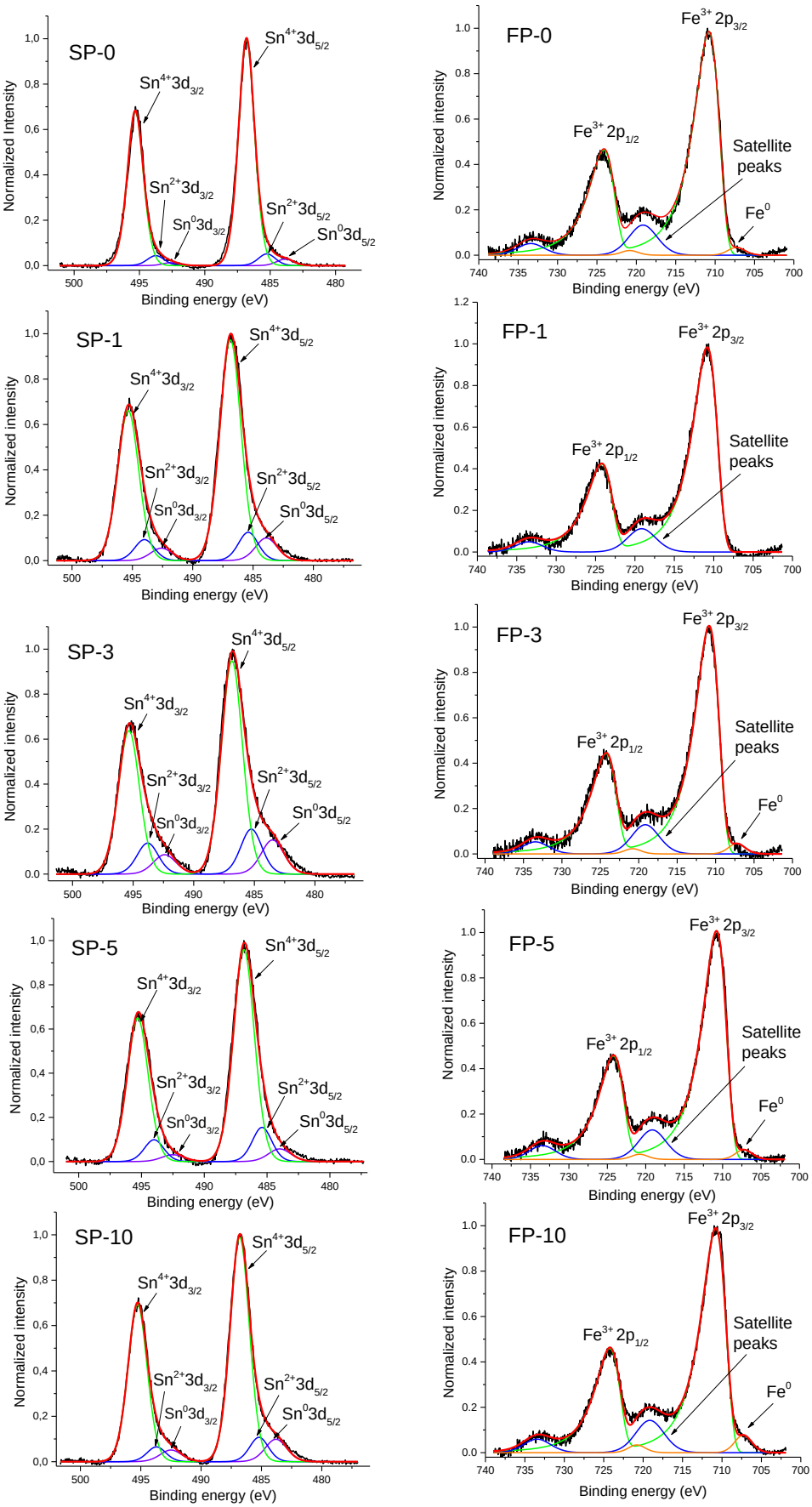

Fig. 7 The Sn 3d and Fe 2p XPS spectra of synthesized samples.

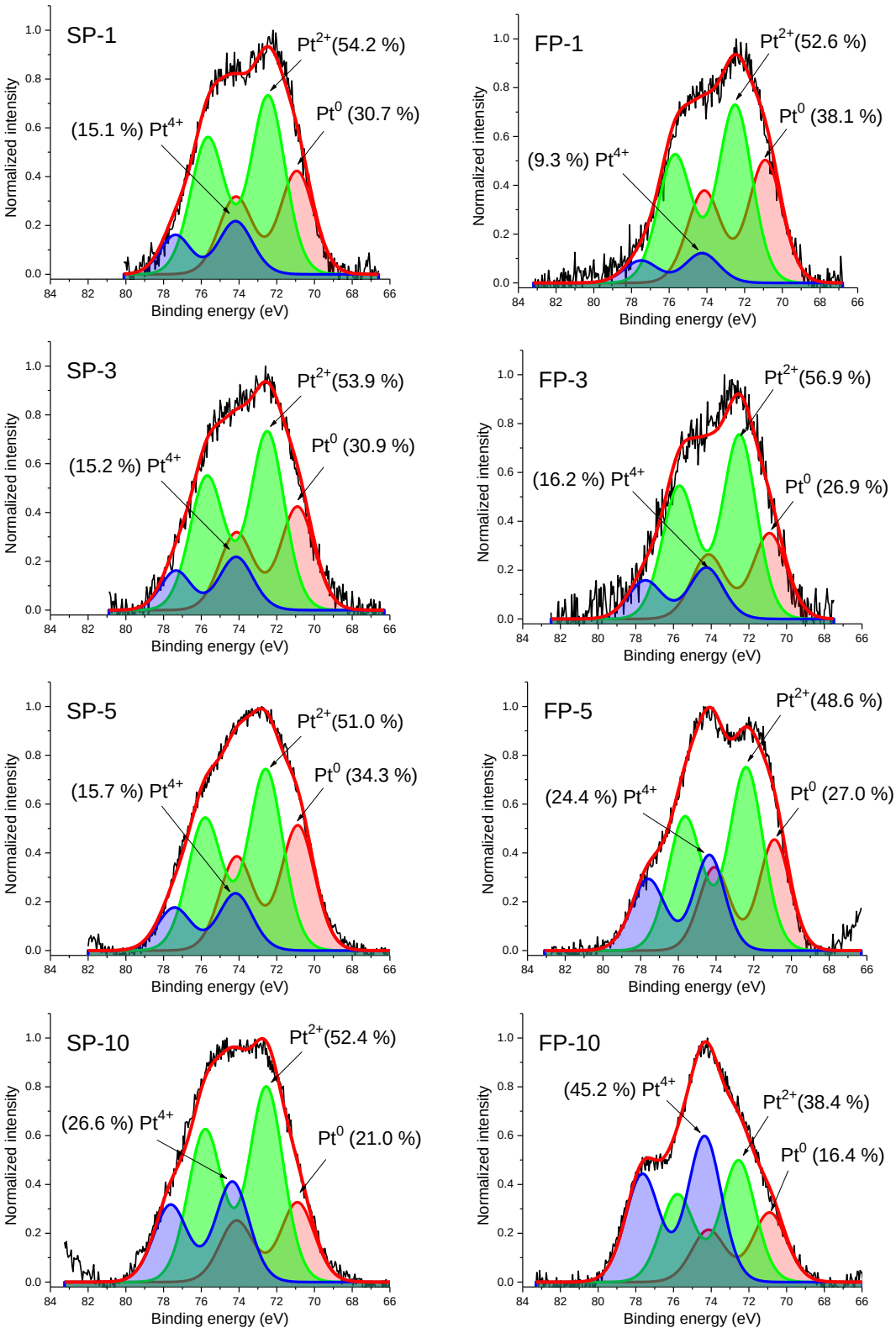

Fig. 8 Pt 4f XPS spectra of synthesized samples.

3.6. UV-Vis results

Fig. 9 shows Tauc plots of calculated from the UV-Vis diffuse reflectance spectra of the synthesized samples. The optical band gap energy of samples was calculated based on the Kubelka-Munk function. The following relation is used:

$$(h\nu\alpha)^{1/n} = A(h\nu - E_g) \quad (1)$$

where h is Planck's constant, ν is frequency, α is absorption coefficient, E_g is band gap and A is proportionality constant. The value of the exponent n represents the type of sample transition (n = 2 for indirect allowed transition, n = 0.5 for direct allowed transition). The calculations were performed for indirect band gap energy determination; therefore, the value of n was set to 2. The collected diffuse reflectance spectra were converted to the Kubelka-Munk function. The vertical axis was converted to a quantity $(h\nu F(R_\infty))^{1/2}$ where $F(R_\infty)$ is proportional to the absorption coefficient and is calculated by the following equation:

$$F(R_\infty) = (1 - R)^2/2R \quad (2)$$

where R is reflectance at a given wavelength. Using the calculated values, $(h\nu F(R_\infty))^{1/2}$ was plotted against hν. A line tangent to the linear part of the curve was extrapolated to zero reflectance. The extrapolated value was used as the optical bandgap energy of the material. The calculated optical band gaps (E_g) of the samples SP-0 to SP-10 were estimated to be between 3.05 and 2.25 eV. The optical band gap of the FP-samples varies around 1.80 eV. The significant change of the optical band gaps with Pt loading in the SP-samples indicates a strong interaction of platinum with the SnO_x support.

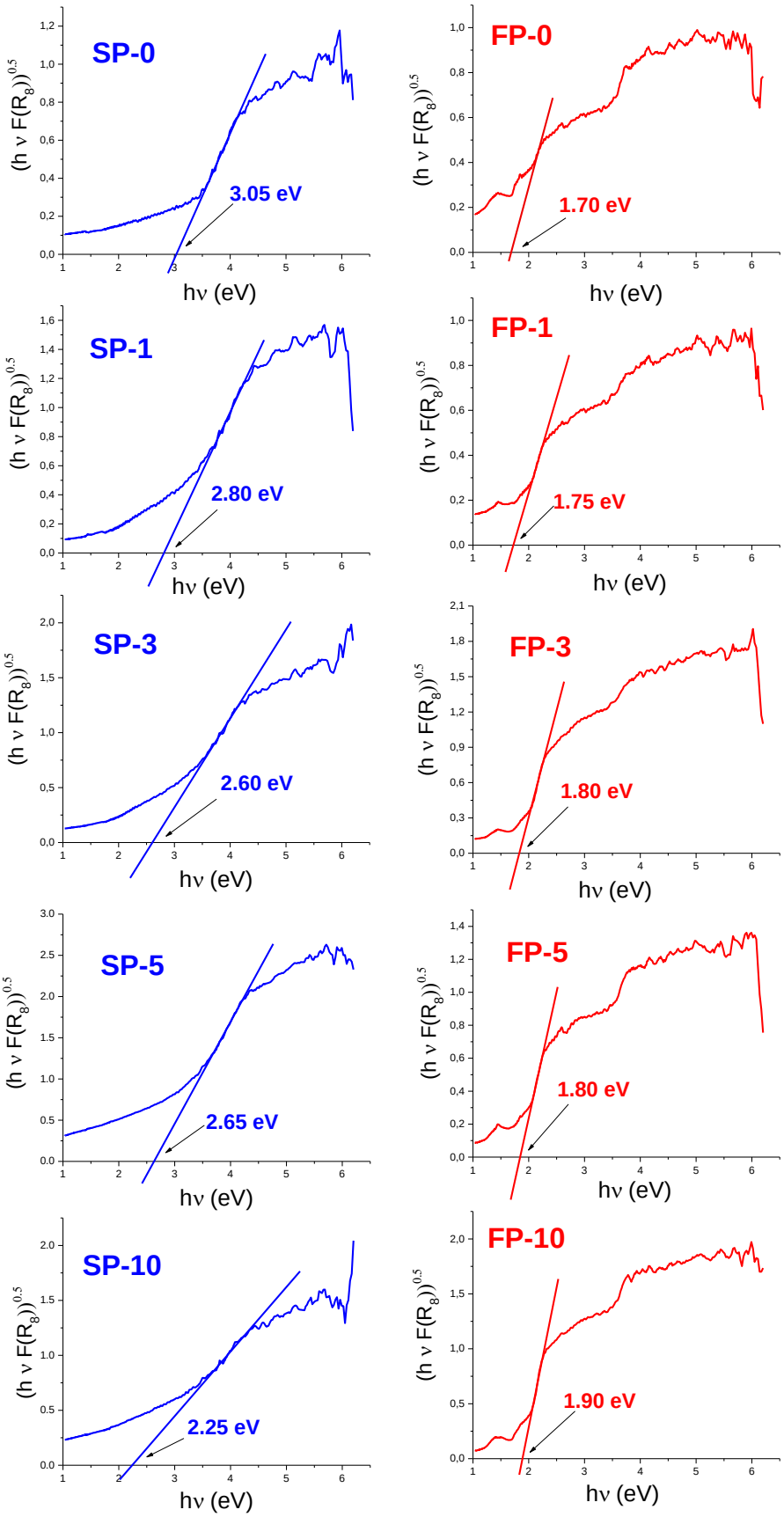

Fig. 9. Tauc plots of the synthesized samples and corresponding optical band gap values.

3.7. Catalytic measurements

Fig. 10 shows the catalytic reduction of 4-nitrophenol (4-NP) to 4-aminophenol (4-AP) in the presence of excess $NaBH_4$ as a function of time using platinum supported on SnO_2 (SP-samples) and α-Fe_2O_3 (FP-samples). The insets show the plot of $\ln(A_t/A_0)$ versus reaction time. Indicated are the values of the rate constant k (s^{-1}) calculated from the slope of the linear segments based on a pseudo-first-order kinetic equation:

$$ln\frac{C_t}{C_0} = ln\frac{A_t}{A_0} = -kt \quad (3)$$

The untreated samples SP-0 and FP-0 to which no platinum was added, are completely catalytically inactive for the reduction of 4-NP to 4-AP (**Fig. S7** in Supplementary Materials). In contrast, the 1 mol% platinum supported on SnO_2 (sample SP-1) showed the highest catalytic activity for the reduction of 4-NP to 4-AP with rate constant k = $1.53 \cdot \times 10^{-2}$ s^{-1}. The catalytic activity was followed by a decrease in absorbance at 400 nm due to 4-nitrophenolate ions and an increase in absorbance at 300 nm due to the formation of 4-aminophenol. Among the FP-samples, the sample supported with 5 mol% platinum (sample FP-5) showed the highest catalytic activity for the reduction of 4-NP with k = $1.11 \cdot \times 10^{-2}$ s^{-1}. The samples with the highest Pt loadings (samples SP-10 and FP-10) showed the lowest catalytic activity for the reduction of 4-NP to 4-AP.

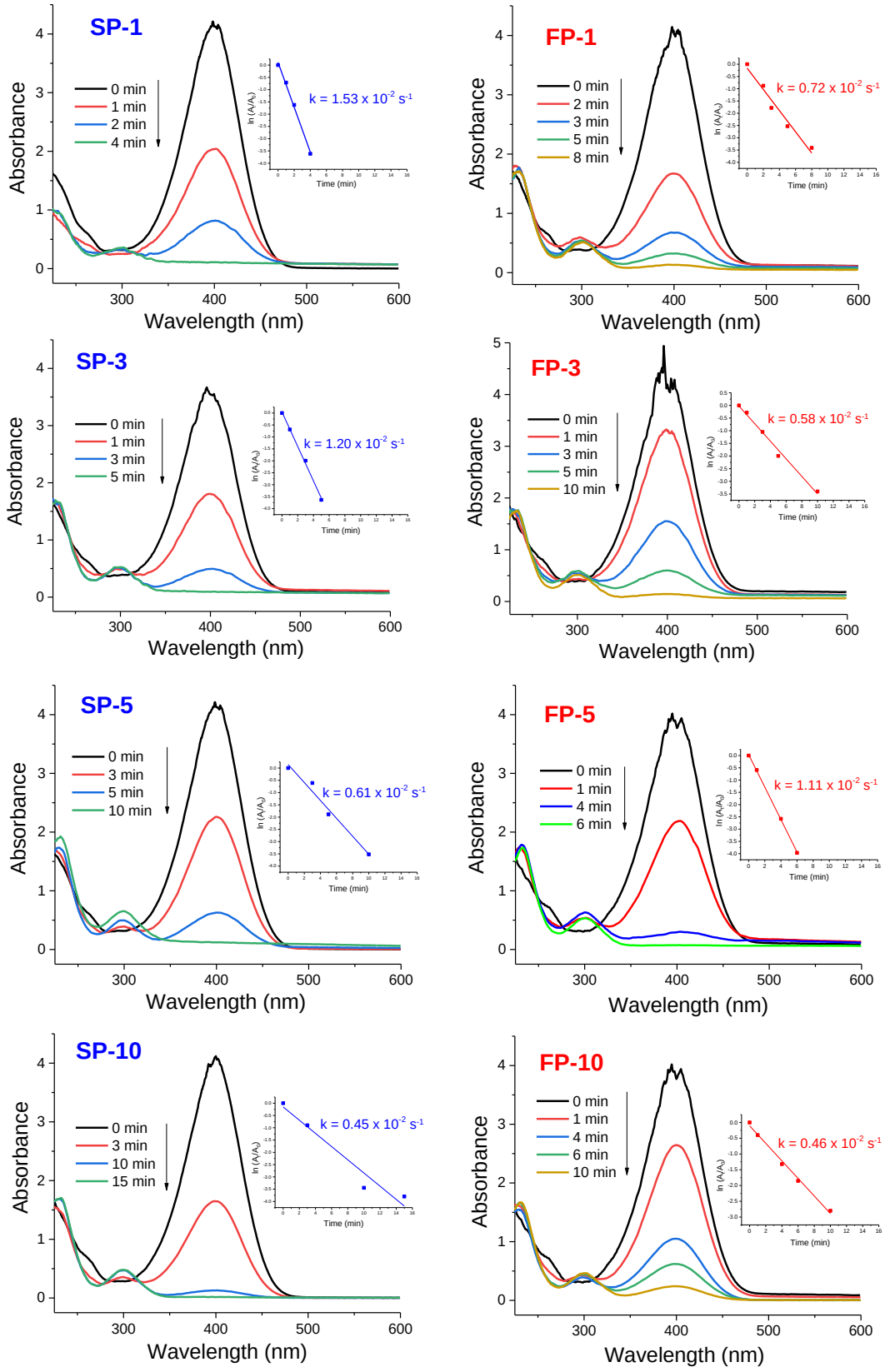

Fig. 10 Catalytic reduction of 4-nitrophenol (4-NP) to 4-aminophenol (4-AP) as a function of time using platinum-decorated SnO_2 (SP) and α-Fe_2O_3 (FP) samples. The insets show the plot of $\ln(A_t/A_0)$ versus reaction time. Indicated are the values of rate constant k (s^{-1}) calculated from the slope of the linear segments.

4. Discussion

Platinum (Pt) is an important catalyst whose catalytic activities depend largely on the degree of dispersion, oxidation state, loading, and choice of support [1-15]. Metal oxide supports such as SnO_2 and α-Fe_2O_3 are thermally stable and reducible compared to inert carbon-based supports with large surface area, and there is a possibility that platinum interacts with metal oxide supports, which can significantly affect the catalytic properties of platinum. We synthesized SnO_2 and α-Fe_2O_3 supports (untreated samples SP-0 and FP-0) by activating Fe(II)acetate and Sn(II)acetate powders in a planetary mill and then annealing at 600 °C. The SnO_2 and α-Fe_2O_3 supports were mixed with $Pt(acac)_2$ powder previously dissolved in a certain volume of toluene. The resulting paste was homogenized in a planetary mill and then annealed at 400 °C, first in an inert atmosphere and then in a stream of oxygen to remove as much of the organic content as possible. In a previous work [17] , we have shown that under similar experimental conditions it is possible to obtain subnanometric PtNPs with a size of 0.8 nm on α-Fe_2O_3 supports, but we have not succeeded in finding PtNPs on SnO_2 supports with a Pt loading of 1 wt%. It should be emphasized that in this previous work we used ball milling with zirconia balls at an extremely high speed of 1000 rpm. Since we did not find any PtNPs, we assumed that because of the similar ionic radii of Sn^{4+} (0.690 Å) and Pt^{4+} (0.625 Å) in the coordination VI, Pt^{4+} can be stabilized in the SnO_2 structure by replacing Sn^{4+} with Pt^{4+} in the crystal lattice, resulting in a $(Pt,Sn)O_2$ solid solution. In this work, stainless steel balls with a rotation speed of only 400 rpm were used. We decided to replace the zirconia balls with stainless steel balls, mainly because of the strong overlap of the Pt M edge at 2.048 keV with Zr Lα edge at 2.042 keV in the EDXS spectra. This overlap makes it very difficult to estimate the relative Pt concentration in the samples.

The detailed XRD analysis using LaB_6 as an internal standard (Figs. 1 and S1 and Tables 1 to 4) showed that the unit cell parameters of hematite (α-Fe_2O_3) and cassiterite (SnO_2) did not change with platinum loading, *i.e.*, there was no replacement of Sn^{4+} by Pt^{4+} in the crystal lattice. The Rietveld refinement results showed two domain sizes (D_v) of cassiterite in the SP samples, the larger one (D_{v1}) with a volume-averaged domain size > 100 nm and the smaller (D_{v2}) with values of about 10 nm (Table 3). The presence of two types of particles in the samples SP-5 and SP-10 is confirmed by the results of STEM, where the small 10 nm in size and the very large irregular plate-like particles larger than 100 nm can be seen in Figs. 3 and 4.

The results from STEM (Figs. 2 and 3) show very good Pt dispersion on both supports, α-Fe_2O_3 and SnO_2, with PtNP size distributions between 1.1 and 1.4 nm and 1.0 and 1.3 nm, calculated with normal and lognormal functions, respectively. The lower Pt loadings (samples SP-1 and FP-1) have smaller PtNP sizes and narrower distributions than the highest Pt loadings (FP-10 and SP-10). The main difference between the Pt dispersion in SP-samples versus FP-samples is the presence of very small spots of about 0.1-0.2 nm in size (Fig. 2), indicating an area of atomically dispersed platinum in the SP-5 sample, while such areas were not found in FP-samples.

The calculated BET surface areas from the N_2 adsorption/desorption isotherms showed that the surface area decreased with platinum loading (Fig. 5), which is consistent with references [27,28] that also observed a decrease in specific surface area with platinum loading. The TPR results make it clear that platinum was reduced well before SnO_2 and α-Fe_2O_3 at about 120-170 °C (Fig. 10). The Sn 3d and Fe 2p XPS results (Fig. 6) indicate that the platinum catalyst interacts more strongly with SP-samples (SnO_2 support) compared to FP-samples (α-Fe_2O_3 support), since despite the fact that Sn^{4+} doublets dominate, Sn^{2+} and Sn^0 doublets are also present. The decrease in the optical band gap from 3.05 eV in the untreated sample SP-0 to 2.25 eV in the sample most heavily loaded with Pt SP-10 (Fig. 9) also indicates strong interactions of platinum with the SnO_2 support. The Pt-4f-XPS results confirm that

platinum dispersed on the SnO_2 and α-Fe_2O_3 supports coexists as Pt^0, Pt^{2+} and Pt^{4+} in all three oxidation states, which can be explained by the strong interaction of platinum with reducible SnO_2 and α-Fe_2O_3 supports [29,30]. The strong interaction of platinum with reducible metal oxide supports has also been noted by other researchers [1,2,11,31–34].

The reduction of 4-NP to 4-AP by sodium borohydride was chosen as a model reaction to test the catalytic performance of Pt/SnO_2 and Pt/α-Fe_2O_3 synthesized samples. An aqueous solution of 4-NP shows a UV absorption maximum at 318 nm (**Fig. S6** in the Supplmentary materials). With the addition of sodium borohydride, the maximum at 318 nm shifts to 400 nm, which is due to the formation of 4-nitrophenolate ions under alkaline conditions by the addition of $NaBH_4$. The untreated samples SP-0 and FP-0 were not able to reduce 4-NP to 4-AP, and accordingly, the intensity of the absorption maximum did not change during the 60 min (Fig. S7). However, the addition of only 1 mg of sample SP-1 (containing only 1 mol% Pt) to 50 ml of the reaction mixture caused the absorption maximum at 400 nm to disappear within four min (Fig. 10). The new maxima at 300 nm were due to the formation of 4-AP. The SP samples with higher Pt loading also reduced 4-NP to 4-AP, but at a slower rate. The apparent rate constant of reduction of 4-NP was calculated assuming pseudo-first order kinetics (Fig. 10 and Table S1). Since the reaction rate is highly dependent on the amount of catalyst used, it is expected that the more highly loaded sample would have higher catalytic activity, but the most highly loaded samples had the lowest rate constants. On the other hand, if we calculate the ratio of k to the total mass of platinum used, defined as k/m (s^{-1} mg^{-1}) for the highly active sample SP-1, and assume that a maximum of 0.015 mg of platinum is contained in 1 mg of added sample SP-1, we obtain a mass-normalized rate constant k/m of 1.02 s^{-1} mg^{-1}, which is almost twice that of the Pt/SnO_2 catalyst prepared by laser ablation of a metallic Sn target in deionized water [35]. Among the FP samples, the best catalytic activity was found for the FP-5 sample with an apparent rate constant of $1.11 \cdot \times 10^{-2}$ s^{-1}.

The extraordinary catalytic activity of platinum on SnO_x and α-Fe_2O_3 supports for the reduction of 4-NP to 4-AP can be explained by the high dispersion of non-aggregated ultrasmall PtNPs on the SnO_x and α-Fe_2O_3 supports. About half of the PtNPs on the supports are subnanometric, *i.e.*, less than 1 nm in size (see particle size distributions), and obviously they are very active and accessible during the catalytic reaction. Moreover, the SP-samples contain Sn^0 and Sn^{2+}, *i.e.*, a reduced SnO_x support. In particular, the SP-3 sample contains more than 10 % Sn^0 and Sn^{2+} (**Table S1** in Supplementary materials) The presence of SnO/SnO_2 in the support may have a positive effect on the catalytic properties of platinum. For instance, Mousavi et al. [36] reported that reduced Pt/SnO_2 sensors used for the detection of pollutants in automotive exhaust significantly improved the sensor response to CO, shortened the recovery times, and dramatically improved the selectivity for CO compared to C_3H_8 and NO due to the formation of a SnO-SnO_2 p-n junction.

The mechanochemical dispersion of platinum starting from fully dissolved ($Pt(acac)_2$) in toluene and the use of Sn(II) and Fe(II) acetate precursors as well as the optimal annealing temperature (400 °C) have a crucial impact on the formation of a reducible support and highly dispersed ultrasmall PtNPs. Acetylacetonate is an anionic bidentate ligand that can limit the crystal growth of platinum, and its thermal decomposition at 400 °C can generate carbon monoxide (CO) that improves the reducing conditions. Apart from these advantages, mechanochemical synthesis inevitably leads to impurities (frictional heat and forces between balls/ball vessel, etc.) due to high-energy ball milling [37–39]. In the present work, balls and vessels made of hardened chromium steel were used. Iron impurities in the Pt/SnO_2 samples were detected by EDXS analysis (Fig. 4). In addition, we found that our Pt/SnO_2 samples (and Pt/α-Fe_2O_3 samples) are magnetic at room temperature, which turns the main weakness of high-energy ball milling (impurities) into an advantage (magnetic impurities), because the samples can be separated from aqueous suspensions with a strong magnet.

5. Conclusions

Platinum was mechanochemically dispersed over reducible SnO_2 and α-Fe_2O_3 supports starting from $Pt(acac)_2$, Sn(II) and Fe(II) acetates.

The PtNPs size distributions calculated with lognormal functions ranged from 1.0 to 1.3 nm. The lower Pt loadings (1 mol%) have smaller PtNP sizes and narrower distributions than the highest Pt loadings (5 and 10 mol%).

The main difference between the Pt dispersion on SnO_2 supports and α-Fe_2O_3 supports is the presence of very small spots about 0.1 nm in size (Figs. 3h and 3i), indicating an area of atomically dispersed platinum in the Pt/SnO_2 sample with 5 mol% Pt, while such areas were not found in the Pt/α-Fe_2O_3 samples.

The platinum catalyst interacts more strongly with the SnO_2 (SnO_x) support than with the α-Fe_2O_3 (FeO_x) support, which is evident from the TPR results (Fig.) and the calculated optical band gaps (Fig.).

The Pt 4f XPS results show that the dispersed platinum on the SnO_x and FeO_x supports consists of all three oxidation states of platinum: Pt^{4+}, Pt^{2+} and Pt^0.

The platinum on SnO_2 and α-Fe_2O_3 shows high catalytic activity for the reduction of 4-NP to 4-AP, which can be explained by the excellent accessibility and high dispersion of the non-aggregated ultrasmall PtNPs on the SnO_x and FeO_x supports.

Platinum loading is not a critical factor for the catalytic reduction of 4-NP to 4-AP, as the lower loaded samples showed better catalytic activity compared to the highest loaded samples. The optimal platinum loading on the SnO_2 support is 1 mol%, while on the α-Fe_2O_3 support the optimal platinum loading is 5 mol%.

Acknowledgments: This work was financially supported by Croatian Science Foundation under the project UIP-2019-04-1195 “Platinum decorated iron tin oxide solid solutions for hydrogen gas sensing“ (HydGasSens) and by Croatian Government and the European Union through the European Regional Development Fund - the Competitiveness and Cohesion Operational Programme (KK.01.1.1.01.0001). The authors thank dr. Matthijs A. van Spronsen for discussions on XPS results.

References:

[1] Q. Tao, J. Song, N. Sun, Y. Ren, L. Xiang, S. Liu, L. Kuai, Boosting the Activity of Single-Atom Pt1/CeO2 via Co Doping for Low-Temperature Catalytic Oxidation of CO, Inorg. Chem. 61 (2022) 11932–11938. doi:10.1021/acs.inorgchem.2c01666.

[2] J. Song, Y. Yang, S. Liu, L. Li, N. Yu, Y. Fan, Z. Chen, L. Kuai, B. Geng, Dispersion and support dictated properties and activities of Pt / metal oxide catalysts in heterogeneous CO oxidation, Nano Res. 14 (2021) 4841–4847. doi:https://doi.org/10.1007/s12274-021-3443-7.

[3] M.E.A. Warwick, D. Barreca, E. Bontempi, G. Carraro, Pt-functionalized Fe2O3 photoanodes for solar water splitting: the role of hematite nano- organization and the platinum redox state, Phys. Chem. Chem. Phys. (2015). doi:10.1039/C5CP01636C.

[4] K. Lakshmi, R. Rangasamy, E.P.A. Sridhar, Immobilization of Pt nanoparticles on magnetite – poly (epoxyamine) nanocomposite for the reduction of p - nitrophenol, SN Appl. Sci. (2019). doi:10.1007/s42452-019-1137-5.

[5] S.C. Ouyang, L.W. Wang, X.W. Du, C. Zhang, J. Yang, In situ synthesis of highly-active Pt nanoclusters via thermal decomposition for high-temperature catalytic reactions, RSC Adv. 6 (2016) 49777–49781. doi:10.1039/c6ra04681a.

[6] H. Cai, H. Liu, T. Ni, Y. Pan, Y. Zhao, Y. Zhu, Controlled Synthesis of Pt Doped SnO2 Mesoporous Hollow Nanospheres for Highly Selective and Rapidly Detection of 3-Hydroxy-2-Butanone Biomarker, Front. Chem. 7 (2019) 1–13. doi:10.3389/fchem.2019.00843.

[7] M. Wagner, N. Waleska, F. Gr, Hybrid Organic − Platinum Nanoparticles for Hydrogenation Reactions, ACS Appl. Nano Mater. 4 (2021) 4329−4334. doi:https://doi.org/10.1021/acsanm.1c00498.

[8] P.M. Bulemo, H.J. Cho, D.H. Kim, I.D. Kim, Facile Synthesis of Pt-Functionalized Meso/Macroporous SnO2 Hollow Spheres through in Situ Templating with SiO2 for H2S Sensors, ACS Appl. Mater. Interfaces. 10 (2018) 18183–18191. doi:10.1021/acsami.8b00901.

[9] A. Martyla, M. Kopczyk, P. Marciniak, R. Przekop, One-pot method of synthesis of Pt/SnO2 system and its electrocatalytic activity, Chem. Cent. J. 8 (2014) 1–10. doi:10.1186/s13065-014-0049-0.

[10] I. Kocemba, J. Rynkowski, The influence of catalytic activity on the response of Pt/SnO2 gas sensors to carbon monoxide and hydrogen, Sensors Actuators, B Chem. 155 (2011) 659–666. doi:10.1016/j.snb.2011.01.026.

[11] M.M. Tellez-Cruz, M.A. Padilla-Islas, M. Pérez-González, O. Solorza-Feria, Comparative study of different carbon-supported Fe2O3-Pt catalysts for oxygen reduction reaction, Environ. Sci. Pollut. Res. 24 (2017) 25682–25692. doi:10.1007/s11356-016-7374-x.

[12] N. An, Q. Yu, G. Liu, S. Li, M. Jia, W. Zhang, Complete oxidation of formaldehyde at ambient temperature over supported Pt/Fe2O3 catalysts prepared by colloid-deposition method, J. Hazard. Mater. 186 (2011) 1392–1397. doi:10.1016/j.jhazmat.2010.12.018.

[13] W. Rachmady, M.A. Vannice, Acetic Acid Hydrogenation over Supported Platinum Catalysts, J. Catal. 334 (2000) 322–334. doi:doi:lO.lOO6/jcat.2000.2863.

[14] H. Wang, K. An, A. Sapi, F. Liu, G.A. Somorjai, Effects of Nanoparticle Size and Metal / Support Interactions in Pt-Catalyzed Methanol Oxidation Reactions in Gas and Liquid Phases, Catal. Letters. 144 (2014) 1930–1938. doi:10.1007/s10562-014-1347-9.

[15] C. Dai, Y. Zhang, J. Chen, X. Zhong, L. Zhang, Support Morphology Effect on Selective Hydrogenation of 3-Nitrostyrene to 3-Vinylaniline over Pt/α-Fe2 O3 Catalysts, Chem. Eur. J. 28 (2022) 1–5. doi:10.1002/chem.202200199.

[16] H. Schreyer, R. Eckert, S. Immohr, J. de Bellis, M. Felderhoff, F. Schüth, Milling Down to Nanometers: A General Process for the Direct Dry Synthesis of Supported Metal Catalysts, Angew. Chemie - Int. Ed. 58 (2019) 11262–11265. doi:10.1002/anie.201903545.

[17] E. Radin, G. Štefanić, G. Dražić, I. Marić, T. Jurkin, A. Pustak, N. Baran, M. Raić, M. Gotić, Solid-State Dispersions of Platinum in the SnO2 and Fe2O3 Nanomaterials, Nanomaterials. 11, 3349 (2021) 1–16. doi:https://doi.org/10.3390/nano11123349.

[18] R.H.T.C.R. Szargan, Peak shape analysis of core level photoelectron spectra using UNIFIT for WINDOWS, (1999) 48–54.

[19] J. Li, Y. Zhang, T. Yi, Z. Zhang, Z. Miao, L. Sun, Z. Zhang, X. Yang, The redispersion behaviour

of Pt on the surface of Fe2O3, RSC Adv. 6 (2016) 25894–25899. doi:10.1039/c6ra01803c.
[20] W. Xia, H. Wang, X. Zeng, J. Han, J. Zhu, M. Zhou, S. Wu, High-efficiency photocatalytic activity of type II SnO/Sn3O 4 heterostructures via interfacial charge transfer, CrystEngComm. 16 (2014) 6841–6847. doi:10.1039/c4ce00884g.
[21] M. Kwoka, L. Ottaviano, M. Passacantando, S. Santucci, G. Czempik, J. Szuber, XPS study of the surface chemistry of L-CVD SnO 2 thin films after oxidation, 490 (2005) 36–42. doi:10.1016/j.tsf.2005.04.014.
[22] J.C. Wang, J. Ren, H.C. Yao, L. Zhang, J.S. Wang, S.Q. Zang, L.F. Han, Z.J. Li, Synergistic photocatalysis of Cr(VI) reduction and 4-Chlorophenol degradation over hydroxylated α-Fe2O3 under visible light irradiation, J. Hazard. Mater. 311 (2016) 11–19. doi:10.1016/j.jhazmat.2016.02.055.
[23] X.F. Lu, X.Y. Chen, W. Zhou, Y.X. Tong, G.R. Li, α-Fe2O3@PANI core-shell nanowire arrays as negative electrodes for asymmetric supercapacitors, ACS Appl. Mater. Interfaces. 7 (2015) 14843–14850. doi:10.1021/acsami.5b03126.
[24] D.L. Peng, K. Sumiyama, M. Oku, T.J. Konno, K. Wagatsuma, K. Suzuki, X-ray diffraction and X-ray photoelectron spectra of Fe-Cr-N films deposited by DC reactive sputtering, J. Mater. Sci. 34 (1999) 4623–4628. doi:10.1023/A:1004638700680.
[25] M. Jansen, B. Yue, Y. Ma, H. Tao, L. Yu, G. Jian, X. Wang, X. Wang, CN x nanotubes as catalyst support to immobilize platinum nanoparticles for methanol oxidation, 18 (2008). doi:10.1039/b718283j.
[26] K. Siuzdak, M. Sawczak, M. Klein, G. Nowaczyk, S. Jurga, A. Cenian, Preparation of platinum modified titanium dioxide nanoparticles with the use of laser ablation in water, Phys. Chem. Chem. Phys. 16 (2014) 15199–15206. doi:10.1039/c4cp01923g.
[27] M. Rahman, K. Inaba, G. Batnyagt, M. Saikawa, K. Higashi, D.T. Uruga, D.Y. Iwasawa, D.K. Ui, supported by high-surface-area activated carbons, (2021) 20601–20611. doi:10.1039/d1ra02156g.
[28] S. Taylor, E. Fabbri, P. Levecque, T.J. Schmidt, O. Conrad, The Effect of Platinum Loading and Surface Morphology on Oxygen Reduction Activity, Electrocatalysis. (2016) 287–296. doi:10.1007/s12678-016-0304-3.
[29] B. Vijay, K. Kaushik, Identification of Mixed Platinum States and Electronic Effects of Support on Platinum in Supported Catalysts *, 113 (1991) 105–113.
[30] M.Y. Smirnov, A. V. Kalinkin, E.I. Vovk, V.I. Bukhtiyarov, Analysis of the oxidation state of platinum particles in supported catalysts by double differentiation of XPS lines, J. Struct. Chem. 57 (2016) 1127–1133. doi:10.1134/S002247661606010X.
[31] M. Liu, W. Tang, Z. Xie, H. Yu, H. Yin, Y. Xu, S. Zhao, S. Zhou, Design of Highly Efficient Pt-SnO2 Hydrogenation Nanocatalysts using Pt@Sn Core-Shell Nanoparticles, ACS Catal. 7 (2017) 1583–1591. doi:10.1021/acscatal.6b03109.
[32] L. Ma, X. Chen, J. Li, H. Chang, J.W. Schwank, Electronic metal-support interactions in Pt/FeOx nanospheres for CO oxidation, Catal. Today. (2019) 1–8. doi:10.1016/j.cattod.2019.06.055.
[33] Z.Z. Jiang, Z.B. Wang, Y.Y. Chu, D.M. Gu, G.P. Yin, Ultrahigh stable carbon riveted Pt/TiO2-C catalyst prepared by in situ carbonized glucose for proton exchange membrane fuel cell, Energy Environ. Sci. 4 (2011) 728–735. doi:10.1039/c0ee00475h.
[34] Y. Shi, Z. Ma, Y. Xiao, Y. Yin, W. Huang, Z. Huang, Y. Zheng, F. Mu, R. Huang, G. Shi, Y. Sun, X. Xia, W. Chen, Electronic metal-support interaction modulates single-atom platinum catalysis for hydrogen evolution reaction, Nat. Commun. 12 (2021) 1–11. doi:10.1038/s41467-021-23306-6.
[35] S. Wu, J. Liu, Y. Ye, Z. Tian, P. Li, Y. Cai, Y. Lin, C. Liang, In-situ reactive loading of platinum onto tin oxide nanocrystals with superior catalytic performance for hydrogenation of 4-nitrophenol, Appl. Surf. Sci. 471 (2019) 469–474. doi:10.1016/j.apsusc.2018.12.035.
[36] H. Mousavi, Y. Mortazavi, A.A. Khodadadi, M.H. Saberi, S. Alirezaei, Enormous enhancement of Pt/SnO2 sensors response and selectivity by their reduction, to CO in automotive exhaust gas pollutants including CO, NOx and C3H8, Appl. Surf. Sci. 546 (2021) 149120. doi:10.1016/j.apsusc.2021.149120.
[37] G. Štefanić, S. Krehula, I. Štefanić, The high impact of a milling atmosphere on steel

contamination, Chem. Commun. 49 (2013) 9245–9247. doi:10.1039/c3cc44803g.
[38] S. Musić, M. Gotić, S. Popović, I. Czakó-Nagy, Formation of γ-Fe2O3 by thermal decomposition of a mixture of Fe(II)- and FE(III)-oxalate salts, Mater. Lett. 20 (1994). doi:10.1016/0167-577X(94)90077-9.
[39] S.G. Sarwat, Contamination in wet-ball milling, Powder Metall. 0 (2017) 1–6. doi:10.1080/00325899.2017.1280647.